

STRUCTURE OF FINAL STATES WITH A HIGH TRANSVERSE MOMENTUM π^0 IN PROTON-PROTON COLLISIONS

P. DARRIULAT, P. DITTMANN, K. EGGERT *, M. HOLDER,
K.T. McDONALD **, T. MODIS ***, F.L. NAVARRIA †, A. SEIDEN ††,
J. STRAUSS, G. VESZTERGOMBI ††† and E.G.H. WILLIAMS
CERN, Geneva, Switzerland

Received 10 March 1976

We present a study of the final state structure in proton-proton collisions ($\sqrt{s} = 53$ GeV) where a large transverse momentum π^0 ($p_{\perp} > 2$ GeV/c) is produced at an angle of 90° . Charged secondaries have been detected and momentum analysed in the split field magnet detector at the CERN Intersecting Storage Rings. The large angular coverage of this detector extends over ± 2.5 units of rapidity and $\pm 30^\circ$ of azimuth with respect to the trigger π^0 , both towards and away from it. In each of these directions, where we observe similar strong correlations, we present charged particle distributions in rapidity and momentum. In the hemisphere containing the trigger π^0 we have measured the cross section for inclusive production of large transverse momentum ρ^\pm mesons. In the opposite hemisphere the data exhibit several features predicted by hard scattering quark-parton models: coplanarity and short-range rapidity correlation for the large transverse momentum secondaries as well as a transverse momentum sharing distribution similar to that observed in deep inelastic electro-production and in e^+e^- collisions.

1. Introduction

High transverse momentum production has provided a novel regime for investigating the hadron-hadron interaction, with a hope of probing the short distance behavior of the fundamental strong forces involved. Theoretically, many approaches have been tried in order to understand this type of event. Among the wide spectrum of possibilities are point-like constituent models of various sorts [1] with their links to the highly successful parton approach used to describe lepton-hadron in-

* Visitor from III. Physikalisches Institut der Technischen Hochschule, Aachen, Germany.

** Present address: Enrico Fermi Institute, University of Chicago, Chicago, Ill. 60637, USA.

*** Visitor from Institut für Hochenergiephysik, Heidelberg, Germany.

† Present address: Istituto di Fisica dell'Università, Bologna, Italy.

†† Present address: University of California, Santa Cruz, Cal. 95064, USA.

††† Visiting Scientist from JINR, Dubna, USSR, on leave from Central Research Institute for Physics, Budapest, Hungary.

clusive cross sections. In these models one has to specify the constituents participating and the forces between these constituents. Other approaches have been through the ideas of high-mass fireballs [2] or hadronic bremsstrahlung [3].

On the experimental front, a wealth of data now exists on single particle inclusive distributions for high transverse momentum (p_t) particles produced in proton-proton collisions [4]. These data however have not been able to select fully among the models and furthermore have not led to a coherent picture of the high transverse momentum process. Multi-particle information has been limited mainly to angular distributions and angular correlations [5,6] among particles produced together with a large p_t particle or to momentum correlations of fast particles [7,8] alongside or directly opposite to such a particle. These experiments, at ISR energies and for π^0 's with p_t of a few GeV/c, have revealed an increase of particle density compared to low p_t production over a wide angular range. To make further progress it is clear that the momentum dependence of these features must be studied. Furthermore the large angular spread over which the effects of large p_t production can be felt indicates that a large angular acceptance is needed to see fully the interesting features.

With these points in mind we have performed an experiment at the split field magnet facility [9], a large acceptance spectrometer at the CERN ISR, to look at the charged particles produced in association with a high p_t π^0 . The π^0 was detected in a lead glass array [10], and data were taken for π^0 production angles of 90° and 45° . Only the 90° data are presented here.

The paper is organized as follows: we discuss first the apparatus and acceptance both for the trigger and for accompanying hadrons. Sect. 3 is on particles in the hemisphere centered on the trigger π^0 and focuses on the transverse momentum and rapidity structure of these particles. A cross section is also given for the production of rho mesons. Next we take up the single particle inclusive distributions of particles in the hemisphere opposite the π^0 and the correlations among these particles.

2. Apparatus

2.1. Lead glass and trigger

Fig. 1 shows a plan view of the apparatus. The lead glass detector [10] is a 1 m^2 hexagonal array of 61 lead glass blocks, each 13.6 cm in diameter, 15 radiation lengths deep and viewed by a 5" phototube. It was located at a center-of-mass angle of 90° and at a distance of 3.6 meters from the intersection region. The lead glass block size and the distance of the array from the beams provide a good efficiency and geometrical acceptance for resolving both gammas from a π^0 decay between 2 and 4 GeV/c. In this range if a single γ from the π^0 hits the lead glass there is about a 50% probability that the other γ will also hit the lead glass. The

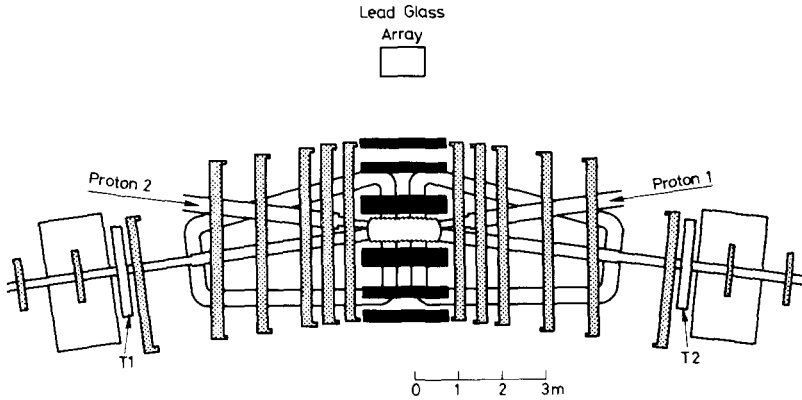


Fig. 1. The split field magnet detector layout. The dotted regions show the chambers of the forward detectors, the black ones show the chambers of the central detector. T1 and T2 are plastic scintillator hodoscopes used to detect small angle secondaries. The position of the lead glass array used to select the high- p_t π^0 trigger is also shown.

separation of these two gammas is always greater than two block diameters and they can be resolved. The procedure used to group the energies deposited in adjacent cells into photon energy clusters, is discussed in ref. [8].

The data presented were all taken at a total center-of-mass energy of 53 GeV. The trigger for the experiment was given by a large energy deposited in the lead glass, as measured by the sum of the phototube dynode signals, in coincidence with a charged particle trigger. The charged particle trigger was made up by requiring signals in at least three chambers in each forward arm of the split field magnet detector (see next section) or a coincidence of scintillators on each side of the proton beam intersect set to view small angle scatters. The cross section seen without the lead glass (minimum-bias trigger) is larger than 90% of the inelastic cross section at this center-of-mass energy. Including the lead glass we get an extremely background free trigger: more than 95% of all triggers are genuine events. For each trigger the split field magnet wire chamber data and the individual lead glass anode pulse heights were recorded on magnetic tape.

In the present analysis we use only those events where both photons of a π^0 are observed separately in the lead glass, thus the π^0 kinematical parameters are known. The cuts used in defining an acceptable π^0 are as follows:

(a) The two γ ray clusters have to be separated by more than two cell diameters (27 cm). This was implemented by only accepting events with a π^0 transverse momentum $p_t^{\pi^0} \leq 4.1$ GeV/c, for which the minimum opening distance is 27 cm. The number of events in our experiment above 4.1 GeV/c is negligible so there is little loss due to this cut.

(b) The energy of each γ ray must be larger than 400 MeV in the laboratory reference frame (~ 460 MeV in the center of mass). This reduces the random background from photons and from charged hadrons, since these normally deposit an

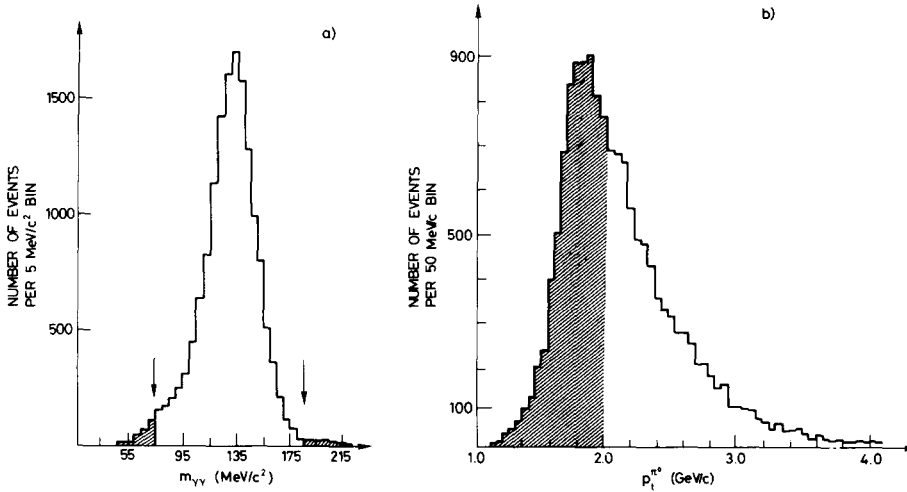


Fig. 2. (a) The two gammas invariant mass distribution for the events selected as described in the text. (b) Distribution of $p_t^{\pi^0}$ in the c.m. system for the selected sample. Events with $p_t^{\pi^0} < 2 \text{ GeV}/c$ are not used in the present work.

energy equivalent of less than 400 MeV. The number of events containing an additional hadron or photon hitting the lead glass is in any case low since the lead glass solid angle is small.

(c) For reconstructed two- γ events the invariant mass $M_{\gamma\gamma}$ of the pair is required to lie between 75 and 185 MeV/c^2 . The number of events with $M_{\gamma\gamma} > 185 \text{ MeV}/c^2$ (three standard deviations away from the peak) is negligible; the cut at 75 MeV/c^2 is chosen to minimize the number of events where a substantial amount of energy leaks out of the edge cells of the lead glass. The average energy shift due to leakage is expected to be 1%.

(d) Events which satisfied the above cuts had their wire chamber information processed through the track finding and reconstruction programs for the split field magnet detector. A final check was then made that no track extrapolated to the lead glass γ clusters. Events which come within 15 cm of one of the two clusters were rejected. The number of such events is 4% of the total. This is done to eliminate most of the events where a γ converts giving incorrect π^0 kinematic parameters.

With these cuts, the distributions in $M_{\gamma\gamma}$ and $p_t^{\pi^0}$ are shown in fig. 2. The lead glass calibration used is described in ref. [11]. The systematic uncertainty in the calibration over the region of interest is 3%. The full width at half maximum of the $M_{\gamma\gamma}$ distribution is 36 MeV/c^2 corresponding to an energy resolution of $\pm 13\%$ on a 1 GeV photon.

In this paper we only use the data with $p_t^{\pi^0} > 2 \text{ GeV}/c$ in the center of mass. (1.7 GeV/c in the lab). This is motivated mainly by the desire to be more fully in

the “high p_t region”, and also by the fact that this cut is well above the lead glass trigger threshold of 1.4 GeV used in the experiment, therefore trigger bias effects [8] are safely ignored. This data sample contains 8019 reconstructed events with $2 \text{ GeV}/c < p_t^{\pi^0} < 4.1 \text{ GeV}/c$. The average value of $p_t^{\pi^0}$ is 2.45 GeV/c.

2.2. Split field magnet detector

The split field magnet and its associated detector is shown in fig. 1. The magnet configuration is such that the field in the right side of the intersect is the return path for the field in the left side of the intersect, and *vice versa*. The pole gap is 1 m and there is an average field of around 1 Tesla in a volume of 20 m^3 . However, the field in the angular region within 15° to the horizontal axis of the magnet, at 90° to the beams, is quadrupole and of much lower average value, which in turn gives poorer momentum resolution.

The multiwire proportional chambers filling the magnet are organized into a forward detector system [9], seeing particles scattered at roughly less than 45° to the beams, and a central detector system [12], set to view particles produced at larger angles. There were however no chambers above or below the beam intersect at the time of the experiment. Both detectors have chambers typically $2 \text{ m} \times 1 \text{ m}$ in area. The wire spacing in the forward chambers is 2 mm while that in the central is 4 mm.

For processing of the wire signal data we have used the pattern recognition and geometrical reconstruction programs Marc and Nicole [13] which have been developed at CERN for the split field magnet facility. We have checked and recalculated the various critical parameters used in these programs. In fig. 3 are shown the average number of wires firing as a function of the track angle with the proportional chamber axis, the resulting error on a measured coordinate at these angles, and the χ^2 probability distribution on the track fits using these errors. The standard deviation on a particle coordinate was measured using field-off data. The chamber alignment was also established using the straight tracks of the same data sample. We successfully processed 90% of all triggers, the 10% lost have many extra wire hits as compared to an average event. An important part of the processing system was a filtering routine developed to delete signals coming from slow spiralling delta rays of which there was typically one per event. This deletion was accomplished by looking for a very high density of signal clusters in a chamber. It has been verified by Monte-Carlo calculation, and more reliably by studying real events, that this procedure causes track losses of less than 3% while increasing the event processing efficiency by 20%.

To check for biases and inefficiencies we have used several features of the pattern recognition program. Tracks which pass through both the central and forward detectors are found first in the forward detector and then extrapolated backwards to the central detector where they are matched with the measured coordinates. This allows a check of the central detector efficiency. To check the forward de-

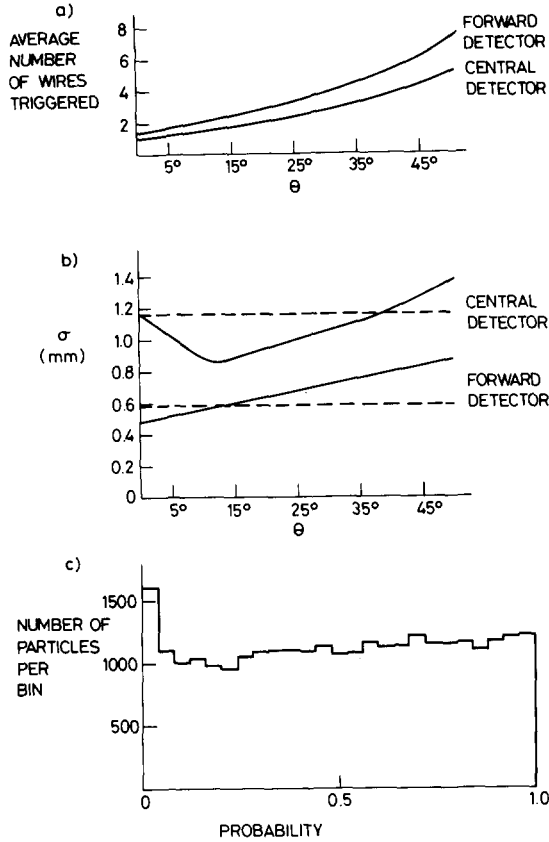


Fig. 3. (a) The average number of wires firing as a function of the angle θ . (b) Error on a measured coordinate in the forward and in the central detectors as a function of the angle between the track and the proportional chamber axis. The dashed lines correspond to the value calculated assuming that only one wire fires independently of the angle. (c) The χ^2 probability distribution for the track fits using the above errors.

tector we selected tracks passing through at least 4 chambers, with a signal missing in one of the planes, and investigated why the coordinate was lost. In addition, we have used data taken with the minimum bias trigger to look for possible inefficiencies. These data have the behaviour expected, namely, an approximately flat rapidity distribution over ± 2 units, a flat azimuthal angle distribution, and a $p_t \exp(-6p_t)$ transverse momentum distribution.

The main losses, besides those due to the geometrical chamber configuration, are due to: interactions in the vacuum pipe or proportional chambers, decays, dead chamber regions due to wire supports every 50 cm, many extra wires firing around a good signal, and cuts in the track finding program. These losses each contribute several percent, giving an average loss of $22\% \pm 5\%$ for particles with momentum

above 250 MeV/c. This loss is rather uniform over the detector. Because of the unusual magnet configuration, there is an additional loss of tracks from poor momentum resolution for small values of the rapidity. In the analysis we discard all tracks with momentum uncertainty $\Delta p/p > 30\%$, resulting in an additional average 10% loss for particles with $p_t \geq 1.5$ GeV/c and $|y| < 0.5$. All these losses have been corrected for by weighting individual particles with the reciprocal of their calculated detection probability. Systematic point to point errors, as well as overall normalization errors, are expected to be less than or equal to 10% in magnitude. The average charged particle multiplicity seen in a high p_t event, before any efficiency correction, is 6.8.

Fig. 4 shows the vertex distribution of the reconstructed events. The shapes seen

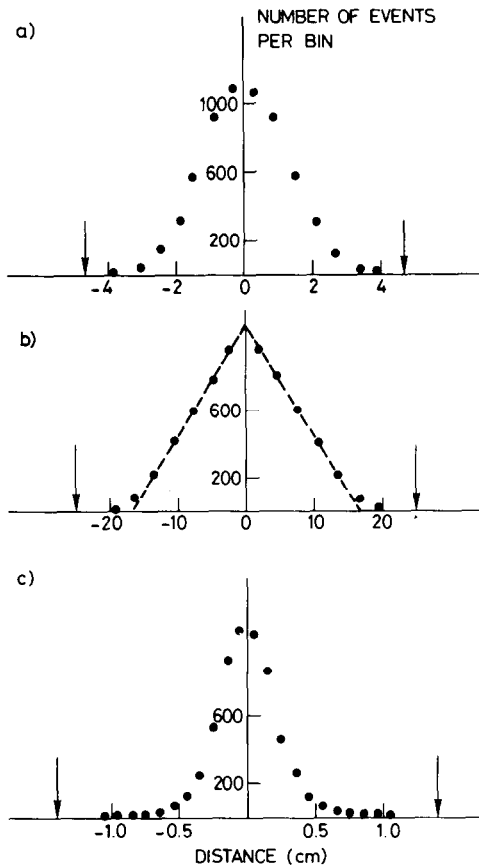


Fig. 4. Vertex distributions of the reconstructed events: (a) Projection on the axis in the plane containing the beams and perpendicular to the beam direction. (b) Projection on the axis along the beam direction. (c) Projection on the vertical axis. The arrows define the regions used in the analysis.

agree with expectations from the dimensions of the proton–proton intersect folded with the errors in determining the vertex location. These errors typically are: 0.7 cm along the average beam direction, 0.4 cm in the horizontal plane perpendicular to the beams, and 0.15 cm in the vertical direction.

2.3. Acceptance and notation

Fig. 5 shows a diagram of the kinematic variables used to describe the hadrons produced in a high $p_t^{\pi^0}$ event. The π^0 and the incoming beams define a scatter plane. The hadron momentum is then broken up into a longitudinal piece, p_y , a piece out of the scatter plane, p_{out} , and a piece opposite the π^0 transverse momentum, p_x . The hadron azimuthal angle, ϕ , is referred to the scatter plane. The rapidity

$$y = \frac{1}{2} \ln \left(\frac{E + p_y}{E - p_y} \right)$$

is calculated assuming all particles to be pions. We will also use a variable $x_e = |p_x/p_t^{\pi^0}|$ to denote how much of the π^0 transverse momentum is balanced by the individual hadrons in the hemisphere opposite to the π^0 . This variable is convenient in understanding how transverse momentum is shared among the accompanying charged particles.

The particles seen in the split field magnet detector will be subdivided into those in the hemisphere centred on the π^0 and those opposite. In the hemisphere opposite the π^0 the region of approximately 100% geometrical acceptance is: $|y| \leq 2.5$, $|180^\circ - \phi| \leq 35^\circ$ and $p_t > 200$ MeV/c. In the hemisphere containing the π^0 the

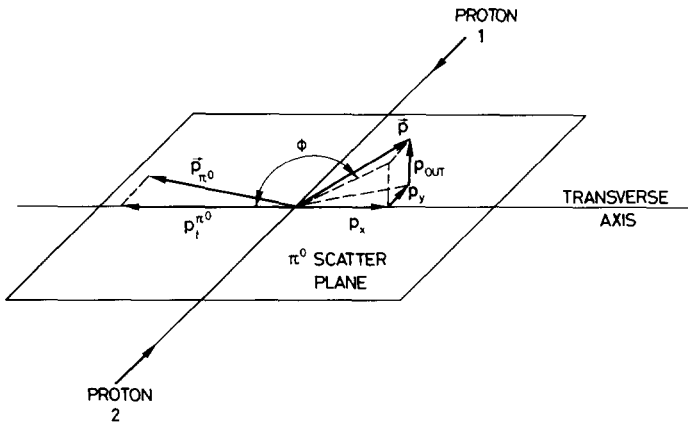


Fig. 5. Diagram showing the kinematic quantities used to describe the triggering π^0 and the secondary hadrons in the c.m. system. The hadron momentum, \mathbf{p} , is broken into three components. The absolute value of the component along the π^0 transverse momentum is called p_x , the one out of the π^0 scatter plane is called p_{out} . The azimuthal angle of the hadron, ϕ , is referred to the π^0 scatter plane which is the plane containing the incoming protons and the π^0 .

analogous region is: $|y| \leq 2$, $|\phi| \leq 27^\circ$, $p_t > 400 \text{ MeV}/c$ ($200 \text{ MeV}/c$ for $|y| < 1$). In these regions nearly all particles pass through at least four wire chamber planes. All particle distributions presented will be restricted to this range and the emphasis will be on charged particles with a large p_t . Because the ϕ acceptance is fixed, there is a limit to how large a p_{out} can be measured for a given value of p_x . Opposite to the π^0 , p_{out} can only be measured up to: $|p_{\text{out}}| \leq 0.7 |p_x|$.

We shall often use as a reference the distributions measured in minimum bias events (no lead glass in trigger). This is suggested by some models [1] and by earlier experimental results [5,6]. The main motivation however, as will be seen, is that this provides a good description of the background under strongly varying features in the data. Although it might be more correct [6] to use minimum bias data taken at an energy $\sqrt{s} - 2p_t^{\pi^0}$, we shall ignore the small correction that it would introduce.

Fig. 6 shows the p_t distribution of particles with $|y| \leq 1$, $p_t > 200 \text{ MeV}/c$ in a

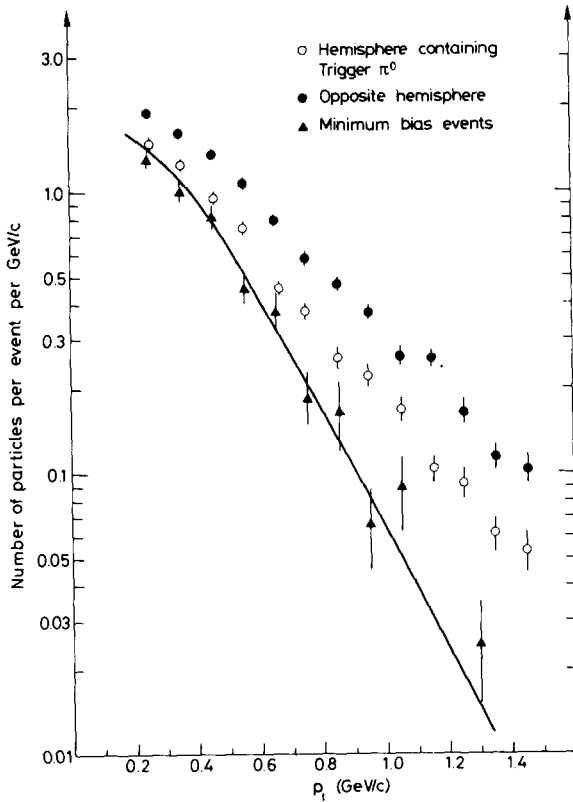


Fig. 6. Transverse momentum distributions for particles with $p_t > 200 \text{ MeV}/c$ accompanying a high $p_t \pi^0$, integrated over rapidity and azimuth with $|y| \leq 1$ and $|\phi|$ or $|180^\circ - \phi| \leq 27^\circ$. The p_t distribution for minimum bias events is also shown with the curve $26 p_t \exp(-6 p_t)$.

$\Delta\phi = \pm 27^\circ$ range in each hemisphere. Also shown is the same distribution in minimum bias events. It can be seen that there is an excess of particles at all momenta in the hemisphere opposite to the π^0 , thus even slow particles participate in the transverse momentum balance. At $p_t \geq 1.2$ GeV/c the ratio between the cross sections observed with and without large p_t production is larger than 5. These considerations dictate the cuts used later to select charged particles from the high p_t process.

3. Charged particle production in the π^0 hemisphere

3.1. Correlations in rapidity and transverse momentum

Each charged particle shall be described, in this hemisphere, by the kinematic variables (y, ϕ, p_x). We use p_x instead of p_t because the trigger π^0 defines a possibly preferred direction; however because of the small ϕ acceptance p_t is always very close to p_x . Integrating over ϕ , the average single particle distribution function is given as $dN/dydp_x$ with normalization equal to the average multiplicity per event, in the region $|\phi| \leq 27^\circ$.

In fig. 7 we show this distribution function integrated over p_x for four bins in p_x between 0.4 and 1.7 GeV/c. Also shown are the same distributions as measured in the minimum bias data. The statistical uncertainty in the minimum bias distributions varies from 10% for the first bin to 20% for the last. The minimum bias background provides a good description, to within 20%, of the flat part of the distribution for all four bins in p_x . This is true over a p_x range in which the minimum bias differential cross section falls by more than a factor of 20. The portion of the distribution above this curve grows with p_x and shrinks in rapidity. For the last bin, $1.1 \text{ GeV/c} < p_x < 1.7 \text{ GeV/c}$, the FWHM of this correlated piece is 0.8 units in y , which corresponds to 25° opening angle between the charged hadron and the π^0 . In the angular region defined as $|y| < 2$ and $|\phi| < 27^\circ$ and for $0.4 \text{ GeV/c} < p_x < 1.7 \text{ GeV/c}$ its integral amounts to 0.13 ± 0.02 charged particles per event. Extending the p_x range down to zero would increase this number by a factor of the order of 3 in agreement with previous observations [5]. The increase of the correlated particle density as a function of p_x had previously been observed in a much smaller rapidity range for accompanying charged particles as well as for π^0 's [7,8].

Also shown in fig. 7 are the associated invariant mass distributions $M(\pi^0, \pi^\pm)$, with a background curve calculated for an uncorrelated minimum bias particle distribution. In these plots, the particles correlated with the π^0 show up as an excess of low mass pairs. These correlated particles are consistent with being distributed in an azimuthal symmetric way around the π^0 direction. The average momentum transverse to the π^0 for these particles is $300 \pm 100 \text{ MeV/c}$ for all p_x .

The charge composition of the particles seen in this hemisphere, in bins of y and p_x , is presented in table 1. The ratio of positives to negatives is everywhere close to unity.

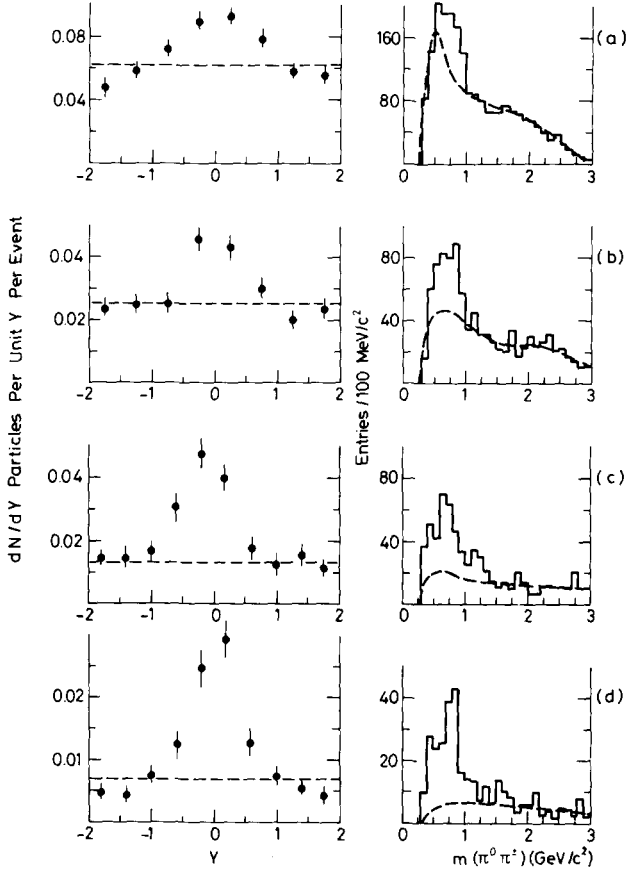


Fig. 7. Rapidity distributions and $\pi^0 - \pi^\pm$ mass distributions for particles in the π^0 hemisphere with $|\phi| \leq 27^\circ$. The data are sliced into different p_X intervals between 0.4 and 1.7 GeV/c: (a) $0.4 < p_X < 0.6$ GeV/c, (b) $0.6 < p_X < 0.8$ GeV/c, (c) $0.8 < p_X < 1.1$ GeV/c, (d) $1.1 < p_X < 1.7$ GeV/c. The mass distributions are plotted for $|y| \leq 2$. The dashed curves show the minimum bias rapidity distributions and the mass distributions expected for uncorrelated particles.

Table 1

Positive to negative charge ratio for various intervals of p_X and y in the π^0 hemisphere

	$0 < y < 0.7$	$0.7 < y < 1.4$	$1.4 < y < 2$
$0.4 < p_X < 0.6$ GeV/c	1.04 ± 0.08	0.93 ± 0.10	1.23 ± 0.13
$0.6 < p_X < 0.8$ GeV/c	0.95 ± 0.09	1.21 ± 0.15	1.26 ± 0.19
$0.8 < p_X < 1.1$ GeV/c	1.04 ± 0.12	1.07 ± 0.22	1.33 ± 0.29
$1.1 < p_X < 1.7$ GeV/c	1.35 ± 0.17	1.19 ± 0.30	1.20 ± 0.39

The ϕ range summed over is $|\phi| < 27^\circ$ for all p_X and y . Systematic errors are not included and are estimated to be less than 10%.

3.2. Production of charged ρ mesons at high p_t

The resolution in mass in the region of the low mass enhancements seen in fig. 7 is typically $\pm 50 \text{ MeV}/c^2$. This excludes that the observed correlation could be solely due to $\pi^\pm \pi^0$ decays of ρ^\pm mesons. However, for the two largest p_x bins there is a signal in the rho mass region. To study this, we take all particles with $0.7 \text{ GeV}/c < p_x < 1.7 \text{ GeV}/c$ and display their invariant mass with the π^0 (fig. 8). With this p_x cut the minimum bias distribution is approximately flat both below and above the rho mass region. The distribution shown has a large excess at the rho mass. The FWHM of the peak is $240 \text{ MeV}/c^2$ which is consistent with the rho width and the errors on the measured π^0 and π^\pm energies and angles. The mass and width of the peak are independent of the π^0 energy.

In order to obtain an estimate of the ρ production cross section, a background was subtracted under the ρ peak as indicated in fig. 8. The detection efficiency of the apparatus within the kinematic region discussed above depends on the transverse momentum of the ρ mesons. For unpolarized ρ 's it rises almost linearly above a threshold of $2.7 \text{ GeV}/c$ and reaches 20% at $p_t = 5 \text{ GeV}/c$. The average observed transverse momentum is $3.5 \text{ GeV}/c$. If the p_t dependences of ρ and π^0 production cross sections in this p_t region are the same, the differential cross section for ρ production can be given simply as a multiple of the π^0 cross section. It is found

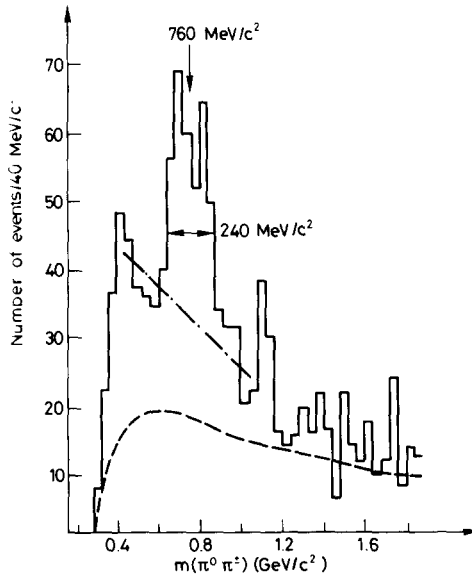


Fig. 8. The $\pi^0 - \pi^\pm$ mass distribution for particles in the π^0 hemisphere, within the limits $|\phi| \leq 27^\circ$, $|y| \leq 2$ and $0.7 < p_x < 1.7 \text{ GeV}/c$. The dashed line is the mass distribution expected for uncorrelated particles and the dashed-dotted line is the background assumed to estimate the ρ signal.

that a parametrization of the form [14]:

$$\frac{d\sigma}{dp_t^2} \propto \frac{1}{(1 + p_t^2)^n} e^{-0.5p_t},$$

with $n = 4.0 \pm 0.6$ describes well the p_t spectrum of the ρ mesons, in agreement with the shape of the π inclusive spectrum. From the observed ρ signal one obtains then a value $\frac{1}{2}(\rho^+ + \rho^-)/\pi^0 = 0.9 \pm 0.2$ for the ratio between the average of the ρ^+ and ρ^- and the direct π^0 production cross section (subtracting the contribution from ρ decays to the π^0 spectrum). If the similarity of ρ and π spectra extends down to $p_t = 2 \text{ GeV}/c$, 16% of the π^0 's studied in this experiment ($p_t \geq 2 \text{ GeV}/c$) are due to ρ meson decays. If we further assume that ρ^0 mesons are produced with the same inclusive cross section as ρ^\pm mesons we can calculate the electron production cross section due to $\rho^0 \rightarrow e^+e^-$ decays. Using a branching ratio [15] of $4.3 \cdot 10^{-5}$ we find an electron to pion ratio of $(0.4 \pm 0.1) \cdot 10^{-5}$. Rho mesons observed in the present experiment generate electrons with a typical transverse momentum of 1.5 to 2 GeV/c .

The detection efficiency of the apparatus depends on the ρ polarization. For a ρ with helicity ± 1 the average detection efficiency is twice as large as for a ρ with helicity 0.

In a similar analysis, from the non-observation of $\omega \rightarrow \pi^+\pi^-\pi^0$ decays we deduce an upper limit of 1.0 (95% confidence level) for the ratio of ω to π^0 productions at an average transverse momentum of 3.5 GeV/c .

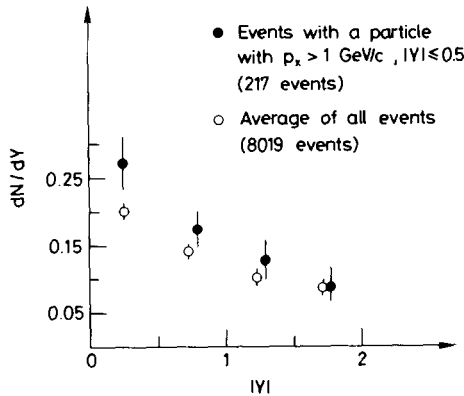


Fig. 9. Rapidity distribution of charged particles in the π^0 hemisphere. The full dots are from events in which a particle with $p_x > 1 \text{ GeV}/c$ and $|y| \leq 0.5$ is observed; this particle is excluded from the plot. The open circles show the distribution of all observed particles in an average large p_t event. Only particles with momenta in the limits $0.4 < p_x < 1.7 \text{ GeV}/c$ have been included.

3.3. Three-particle correlations

For large p_x values, there is a strong rapidity correlation between the charged particles and the π^0 (fig. 7). Does this two-body correlation account fully for the structure in the trigger hemisphere, or is there, event by event, more than one single charged particle correlated to the trigger π^0 ? To answer this question we select events in which a particle is produced with $p_x > 1$ GeV/c, $|y| \leq 0.5$. The rapidity distribution of all the other particles is shown in fig. 9. Also shown is the distribution of all particles in an average large p_t event with neither selection nor deletion of tracks. In the events with a large p_x particle, the remaining particles show at least as strong a correlation as in the average event, giving evidence for a three-particle correlation.

4. Charged particle production in the hemisphere opposite to the π^0

4.1. Rapidity distribution

We now study the rapidity distribution of charged particles produced in the hemisphere opposite to the π^0 , and in particular its dependence upon charge, upon p_x and upon $p_t^{\pi^0}$. In analogy with the study in the π^0 hemisphere we consider a distribution function $dN/dydp_x$, however summed over a wider ϕ range defined as $|180^\circ - \phi| \leq 35^\circ$.

Fig. 10a shows this distribution integrated over p_x between 0.2 and 0.6 GeV/c. In this low p_x range the distributions in rapidity are approximately the same for both positive and negative charges. The ratio of positives to negatives is listed in table 2 for various intervals of y and p_x .

Rapidity distributions for large p_x particles (1.1 GeV/c $\leq p_x \leq 1.7$ GeV/c) are shown in fig. 10b for positive and negative charges separately. The rapidity distribution for positives has approximately the same shape as that of low p_x particles, while negatives fall below this distribution at large rapidities. This results in a large

Table 2
Positive to negative charge ratio for various bins in p_x and y in the hemisphere opposite the π^0

	$0 \leq y \leq 0.6$	$0.6 \leq y \leq 1.2$	$1.2 \leq y \leq 1.8$	$1.8 \leq y \leq 2.5$
$0.2 \leq p_x \leq 0.6$ GeV/c	1.10 ± 0.04	1.25 ± 0.04	1.13 ± 0.04	1.31 ± 0.04
$0.6 \leq p_x \leq 0.8$ GeV/c	1.08 ± 0.07	1.21 ± 0.07	1.42 ± 0.09	2.09 ± 0.21
$0.8 \leq p_x \leq 1.1$ GeV/c	1.29 ± 0.11	1.47 ± 0.10	1.48 ± 0.13	2.07 ± 0.23
$1.1 \leq p_x \leq 1.7$ GeV/c	1.21 ± 0.12	1.46 ± 0.14	1.60 ± 0.17	2.35 ± 0.24

The ϕ range summed over is $|180^\circ - \phi| < 35^\circ$. Systematic errors are not included and are estimated to be less than 10%.

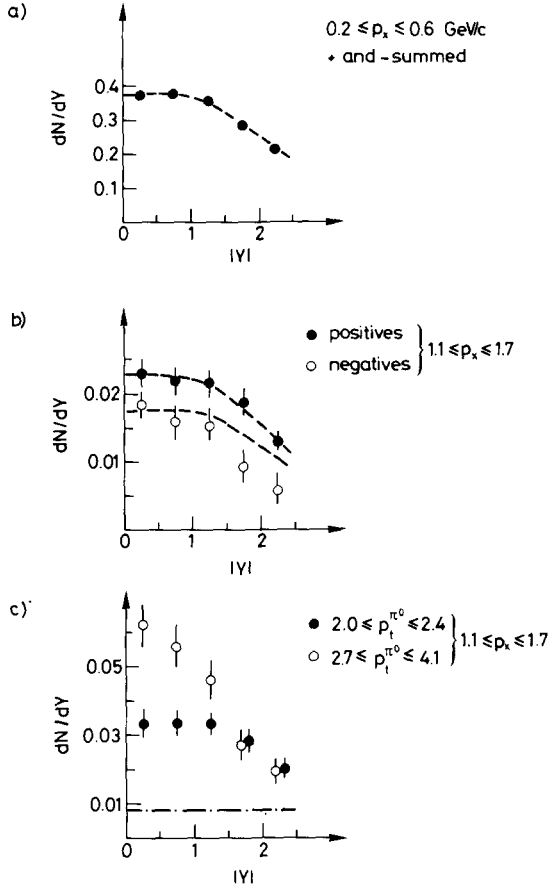


Fig. 10. Distributions of the absolute value of the rapidity for charged particles in the hemisphere opposite the π^0 , with $|180^\circ - \phi| < 35^\circ$. (a) Summed over positive and negative charges for $0.2 < p_x < 0.6 \text{ GeV}/c$. The dashed line is drawn to guide the eye. (b) Broken into positive and negative charges for $1.1 < p_x < 1.7 \text{ GeV}/c$. The dashed lines are the same curve as in (a) but scaled down to agree with the data in the $|y| \leq 1$ region. (c) Broken into two $p_t^{\pi^0}$ intervals, $2 < p_t^{\pi^0} < 2.4 \text{ GeV}/c$ and $2.7 < p_t^{\pi^0} < 4.1 \text{ GeV}/c$, and summed over charges for $1.1 < p_x < 1.7 \text{ GeV}/c$. The dashed-dotted line indicates the mean particle density from minimum bias events.

positive to negative ratio at large p_x and large y . The ratios in table 2 can be compared with those for inclusive distributions at various values of p_t and y [16]. They are not much affected by the requirement of a high $p_t^{\pi^0}$ trigger in the present data. They take values of about 1.1 in the low p_x , low y region, reach values of 1.4 to 1.5 when only one of these parameters is increased, and values around 2 in the large p_x , large y region. At least in the case of inclusive production the excess of positives at higher rapidities is known to be mostly due to the proton component.

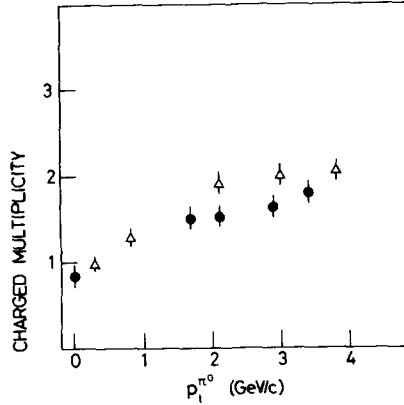


Fig. 11. Number of charged particles per event as a function of $p_t^{\pi^0}$ including the minimum bias value (shown at $p_t^{\pi^0} = 0$) for $180^\circ - \phi \leq 30^\circ$ and $|y| \leq 1$ (full dots). Also shown (open triangles) are data from ref. [5].

We now study the dependence of the rapidity distribution upon $p_t^{\pi^0}$. For low p_x particles ($0.2 \text{ GeV}/c \leq p_x \leq 0.6 \text{ GeV}/c$) its shape remains unchanged, to within the 7% statistical accuracy, when $p_t^{\pi^0}$ varies between 2 and 4.1 GeV/c. Rapidity distributions of large p_x particles are shown in fig. 10c for two different intervals of $p_t^{\pi^0}$ (2 to 2.4 GeV/c and 2.7 to 4.1 GeV/c respectively). For higher $p_t^{\pi^0}$ there are more high p_x charged hadrons which populate mostly the region $|y| \leq 1.5$, the distribution for $|y| > 1.5$ being independent of $p_t^{\pi^0}$ within statistics. The dependence of the positive to negative ratio upon p_x and y is the same in both intervals of $p_t^{\pi^0}$. To further illustrate the increase of particle density at higher $p_t^{\pi^0}$ we consider a region $|y| \leq 1$, $180^\circ - \phi \leq 30^\circ$, where the present data can be compared with earlier results [5], and show in fig. 11 the dependence of the charged particle multiplicity in that region upon $p_t^{\pi^0}$. An 8% correction has been applied to the data to account for the loss of very slow particles ($p_x < 0.2 \text{ GeV}/c$). At $p_t^{\pi^0} = 2.5 \text{ GeV}/c$ the multiplicity in the region considered is twice as large as for “minimum bias” triggers.

4.2. Distribution in p_{out}

Azimuth distributions for charged particles in the hemisphere opposite to the trigger π^0 are shown in fig. 12 for various intervals of their transverse momentum p_t . The $16 \pm 5\%$ drop observed over the ϕ range of the experiment for the low p_t component is in agreement with the data of ref. [5] where the particles were not momentum analysed. As p_t rises, the azimuthal distributions shrink, indicating that particles with high p_t are more coplanar than those with low p_t . In order to describe this effect quantitatively, we concentrate on the distribution in p_{out} (the momentum out of the scatter plane) for large values of p_x . This distribution can

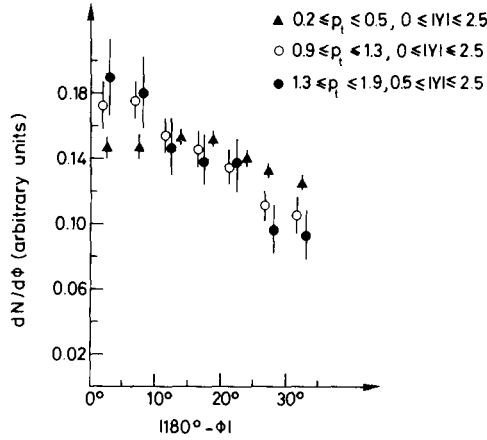


Fig. 12. Azimuth distributions of charged particles with $|y| \leq 2.5$ in the hemisphere opposite the π^0 for various p_t intervals of the charged secondaries. In the highest p_t interval, $1.3 < p_t < 1.9$ GeV/c, the y range is further restricted to $|y| \geq 0.5$ to stay in a region where the detection efficiency is uniform and near its average value. The distributions are normalized to the same area in the ϕ range $|180^\circ - \phi| \leq 35^\circ$.

be fit to an empirical form

$$\frac{dN}{dp_{out}} \propto \exp(-B|p_{out}|) .$$

The result of these fits is presented in fig. 13 and in more detail in table 3. We find $\langle p_{out} \rangle = B^{-1} \simeq 0.50 \pm 0.05$ GeV/c for a wide range of p_x and, in a first approximation, independent of rapidity and charge. In minimum bias events we find instead

$$\langle p_{out} \rangle \simeq 0.6 p_x^{1/2} \quad (p_{out}, p_x \text{ in GeV/c}) ,$$

where p_{out} is defined with respect to an arbitrary scatter plane.

Table 3

Fits to distribution in $|p_{out}|$ of the form: $dN/d|p_{out}| \propto e^{-B|p_{out}|}$

p_x range (GeV/c)	$\langle p_x \rangle$	$ y $ range	Charge	$ p_{out} $ range (GeV/c)	$B = \frac{1}{\langle p_{out} \rangle}$ (GeV/c) ⁻¹	χ^2/DF
$1.1 \leq p_x \leq 1.43$	1.17	$0 \leq y \leq 2.5$	+ and -	$0.1 \leq p_{out} \leq 0.7$	2.1 ± 0.2	0.9
$1.43 \leq p_x \leq 1.72$	1.54	$0 \leq y \leq 2.5$	+ and -	$0.1 \leq p_{out} \leq 1.0$	2.3 ± 0.3	0.4
$1.72 \leq p_x \leq 3.2$	2.13	$1 \leq y \leq 2.5$	+ and -	$0 \leq p_{out} \leq 1.2$	1.7 ± 0.4	0.3
$1.15 \leq p_x \leq 1.7$	1.35	$0 \leq y \leq 1.0$	+ and -	$0.1 \leq p_{out} \leq 0.8$	2.4 ± 0.3	0.6
$1.15 \leq p_x \leq 1.7$	1.35	$1 \leq y \leq 2.5$	+ and -	$0.1 \leq p_{out} \leq 0.8$	2.0 ± 0.3	1.1
$1.15 \leq p_x \leq 1.7$	1.35	$0 \leq y \leq 2.5$	+	$0.1 \leq p_{out} \leq 0.8$	2.1 ± 0.3	1.0
$1.15 \leq p_x \leq 1.7$	1.35	$0 \leq y \leq 2.5$	-	$0.1 \leq p_{out} \leq 0.8$	2.2 ± 0.4	0.2

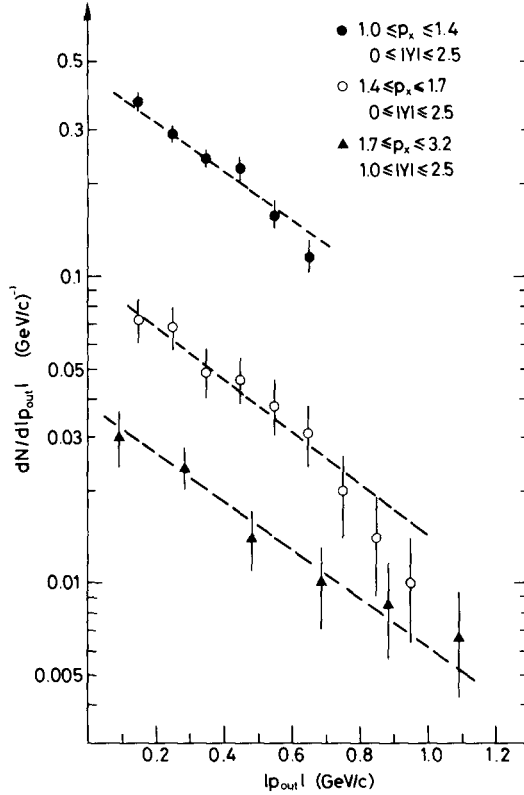


Fig. 13. Distributions of $|p_{\text{out}}|$ for different p_x intervals of the charged particles. The distributions are integrated over y for $|y| < 2.5$, for the highest p_x interval the y range is restricted to $1 \leq |y| \leq 2.5$. The dashed lines correspond to a function

$$dN/d|p_{\text{out}}| \propto \exp(-2|p_{\text{out}}|) .$$

4.3. Distribution in x_e

Transverse momentum balance in a high p_t process is conveniently described by the distribution in $x_e = |p_x/p_t^{\pi^0}|$ integrated over a wide angular range in the hemisphere opposite to the high p_t trigger. We concentrate on charged particles with $1.2 \text{ GeV}/c < p_x < 3.2 \text{ GeV}/c$ and study their x_e distribution in a region of good acceptance defined as $|y| < 2.5$ and $|p_{\text{out}}| < 840 \text{ MeV}/c$. Using $dN/dp_{\text{out}} \propto \exp(-2|p_{\text{out}}|)$, independent of x_e , we apply a 22% correction factor for data lost at $|p_{\text{out}}| > 840 \text{ MeV}/c$. Considering a limited p_x interval helps in sorting out particles involved in the high p_t process but implies that each bin of x_e covers only part of the range in $p_t^{\pi^0}$: each bin is therefore separately normalized to the number of events that can contribute to it.

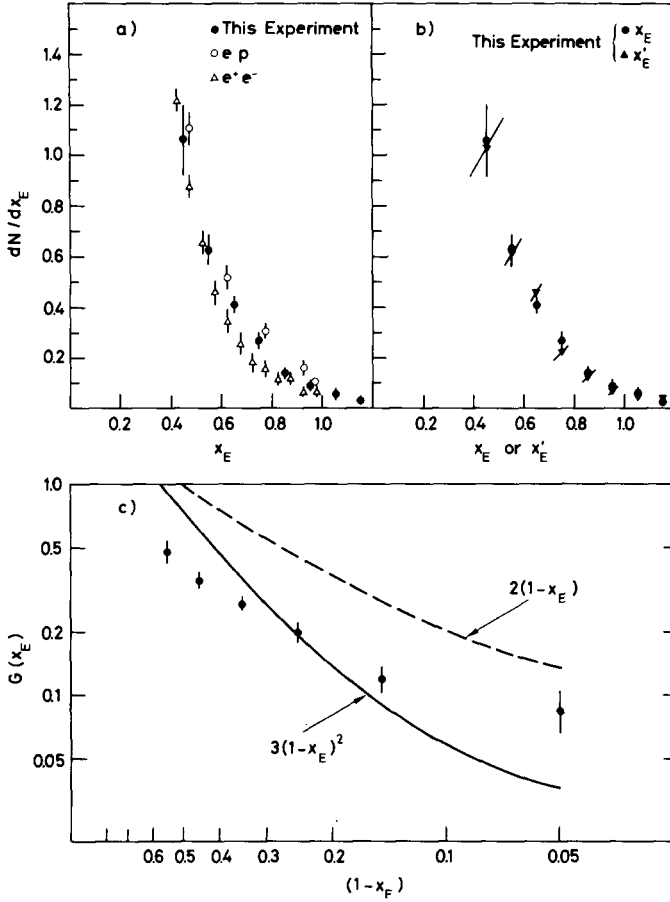


Fig. 14. (a) x_e distribution (see text). The deep inelastic electron scattering data [16] were taken at c.m. energies between 3.5 and 5.5 GeV and in the range $1 < q^2 < 2$ (GeV/c)². For the e⁺e⁻ data [17] we plot $\frac{1}{2}dN/dz$ at $E_{c.m.} = 4.8$ GeV. All the distributions are summed over positive and negative charges and the error bars are purely statistical. (b) Comparison between the x_e and the x'_e distributions (see text). (c) Distribution of $G(x_e) = x_e dN/dx_e$. The full line corresponds to $2(1-x_e)$, the broken one to $3(1-x_e)^2$, both curves are folded with the experimental resolution.

The resulting distribution is shown in fig. 14a, for positive and negative particles together. The average $p_t^{\pi^0}$ varies from 3.3 GeV/c to 2.3 GeV/c across the x_e range. The distribution is steeply falling with x_e and has an integral of 0.25 for $x_e \geq 0.4$. This means that on the average 25% of the events have one charged particle which balances more than 40% of the transverse momentum $p_t^{\pi^0}$ of the trigger π^0 .

Also shown in fig. 14a are the distribution in the Feynman x_F variable (p_{\perp}/p_L^{\max} in the proton-virtual photon c.m. system) measured for final state hadrons in deep inelastic electro production [17] and a similar distribution in $z = p/p_{\max}$ for hadrons

produced in e^+e^- annihilation at 4.8 GeV c.m. energy [18]. These three distributions, in x_e , x_F and z , are strikingly similar in shape and magnitude. In quark-parton models [1], where the hadrons in the final state are the decay products of a large transverse momentum quark, all the above distributions measure the probability that the quark fragments into a hadron of fractional momentum x_e , or x_F , or z , and are therefore expected to be identical, to the extent that quarks of the same types are involved in the three processes. To account for a possible difference in the isospin content of the scattered quark, we have summed over positive and negative charges before making the comparison. Also of relevance is the question whether specific states, such as diffractive vector meson production for the deep inelastic process, should be excluded. These states in fact account for most of the excess in the x_F distribution (at large x_F), as compared to the x_e distribution. Finally we tacitly implied that the trigger π^0 carries all the relevant p_\perp in its hemisphere and exactly balances the quark transverse momentum. This is not quite correct since particles correlated with the π^0 are clearly seen in its own hemisphere. In fact we observe that a larger fraction of the events with a large x_e particle have a fast particle accompanying the π^0 in its hemisphere as well, as compared to an average event (table 4). Nevertheless, probably because the trigger strongly emphasizes events where the π^0 carries most of the transverse momentum in its hemisphere, this does not strongly affect the x_e distribution. To illustrate this, we redefine x_e as $x'_e = |p_x|/(p_\perp^{\pi^0} + p'_x)$ for a certain fraction of events in which there is a fast track close to the π^0 , with rapidity $|y'| < 1$ and with $p'_x > 0.4$ GeV/c. This fraction is defined from the surplus of high p_\perp events above the observed level of minimum bias events in the rapidity distributions of fig. 7. The distribution in x'_e is shown in fig. 14b and does not substantially differ from that in x_e .

Because of the limited $p_\perp^{\pi^0}$ range of present data and the acceptance limitations outlined earlier, we cannot study the dependence of the x_e distribution on $p_\perp^{\pi^0}$. In a coplanar two-jet model, where hadrons in each hemisphere come from independent fragmentation of each jet, one might expect the x_e distribution to be independent of $p_\perp^{\pi^0}$.

We display, for completeness, the function $G(x_e) = x_e dN/dx_e$ in fig. 14c. This is motivated by the fact that parton models [1] predict such a $1/x$ form for dN/dx , with $\int_0^1 G(x_e) dx_e = 1$. We show the dependence of $\log(G(x_e))$ upon $\log(1 - x_e)$

Table 4

Fraction f of events with a fast charged particle ($p_x > 1$ GeV/c) produced in the neighbourhood ($|y| < 0.5$) of the trigger π^0 as a function of x_e of the largest x_e charged particle in the opposite hemisphere

x_e range	f (%)
all events	$(4.5 \pm 0.5)\%$
0.4 to 0.6 ($p_x > 1.2$ GeV/c)	$(7.8 \pm 1.6)\%$
above 0.85	$(13.6 \pm 3.9)\%$

Table 5

Hemisphere multiplicities for various intervals of x_e of the largest x_e charged particle in the hemisphere opposite the trigger π^0

x_e range	Multiplicity in the π^0 hemisphere	Multiplicity in the opposite hemisphere
0 to 0.4	1.21 ± 0.03	3.33 ± 0.03
0.4 to 0.6	1.46 ± 0.05	4.03 ± 0.05
0.6 to 0.8	1.46 ± 0.08	4.12 ± 0.10
> 0.8	1.69 ± 0.12	3.81 ± 0.13
Minimum bias events with at least one particle in the hemisphere opposite the trigger π^0	1.11 ± 0.05	2.47 ± 0.05

Multiplicities are summed over a region $|\eta| < 2$, $|\phi| < 27^\circ$ for the π^0 hemisphere and $|\eta| < 2.5$, $|\phi - 180^\circ| < 35^\circ$ for the opposite hemisphere. No correction has been applied to account for the loss of slow particles in either hemisphere due to the acceptance of the detector. For a $p_t \exp(-6p_t)$ distribution this amounts to 40% in the π^0 hemisphere and 10% in the opposite hemisphere.

to better demonstrate the behaviour of this function in the vicinity of $x_e = 1$ and to permit comparison with $(1 - x_e)^p$ laws.

In table 5 we list the hemisphere multiplicities *versus* the x_e of the largest x_e particle in the hemisphere opposite the trigger π^0 . A clear rise is observed, in the π^0 hemisphere, when x_e increases.

4.4. Two-particle correlations

The observation that large p_t secondaries in the hemisphere opposite to the trigger π^0 inclusively cover a wide range in rapidity does not imply that the same is true in each event separately. In particular it might be that large p_t secondaries are produced in a rather narrow jet, but that the axis of the jet spans a wide rapidity range from event to event. With this question in mind we select events where the particle with the largest value of x_e in the hemisphere opposite to the trigger π^0 satisfies the inequality $p_x > 1.2 \text{ GeV}/c$ and lies in a given rapidity interval. For these events we study the rapidity distribution of the other particles, leaving out that with the largest x_e . The result is shown in fig. 15 for three different rapidity intervals of the particle with the largest x_e . We observe that particles accompanying a large x_e product are shifted in rapidity towards the direction of the large x_e product, the shape of their rapidity distribution being different for the three rapidity intervals of the large x_e product. The structure in these data suggests that a fraction of the particles is closely correlated to the particle with the largest x_e , and another fraction is more or less uniformly distributed over the available rapidity range. The size and shape of this correlation can be better demonstrated by combining the data with different rapidities of the particle with the largest x_e . Fig. 16

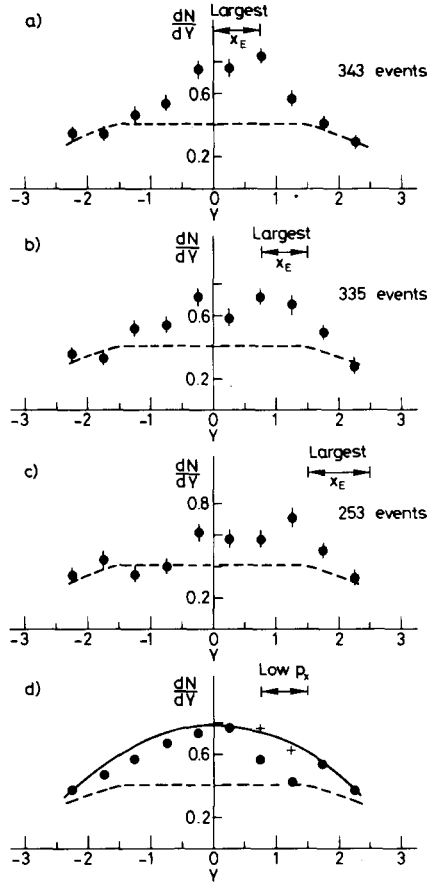


Fig. 15. Rapidity distributions of charged particles in the hemisphere opposite the π^0 . All particles are plotted without cuts in p_x and about 10% of the particles are estimated to be lost because they are very slow. (a), (b) and (c) Selecting events with a fast particle, $p_x > 1.2$ GeV/c, within different rapidity intervals: $0 \leq |y_{\text{fast}}| \leq 0.75$, $0.75 \leq |y_{\text{fast}}| \leq 1.5$ and $1.5 \leq |y_{\text{fast}}| \leq 2.5$ respectively. The fastest particle is not included in the plots. If the fastest particle has negative y_{fast} the plotted value is actually $-y$. The dashed lines show the rapidity distribution observed in minimum bias events. (d) Selecting events in which a low p_x particle, $p_x < 0.6$ GeV/c, occurs with $0.75 \leq y \leq 1.5$. The low p_x particle is not plotted. The dashed line is the rapidity distribution for minimum bias events and the solid line is the rapidity distribution observed in an average high- p_t π^0 event.

shows the density of additional particles within $|y| < 2.25$ for events which have at least one large p_x particle ($p_x > 1.2$ GeV/c) in the rapidity interval $|y_{\text{fast}}| < 1.5$. It can be decomposed into a background proportional to the uncorrelated particle density and an excess at small rapidity differences. This excess extends over ± 0.6 units of rapidity (σ) and contains 0.33 ± 0.07 particles per event. For comparison

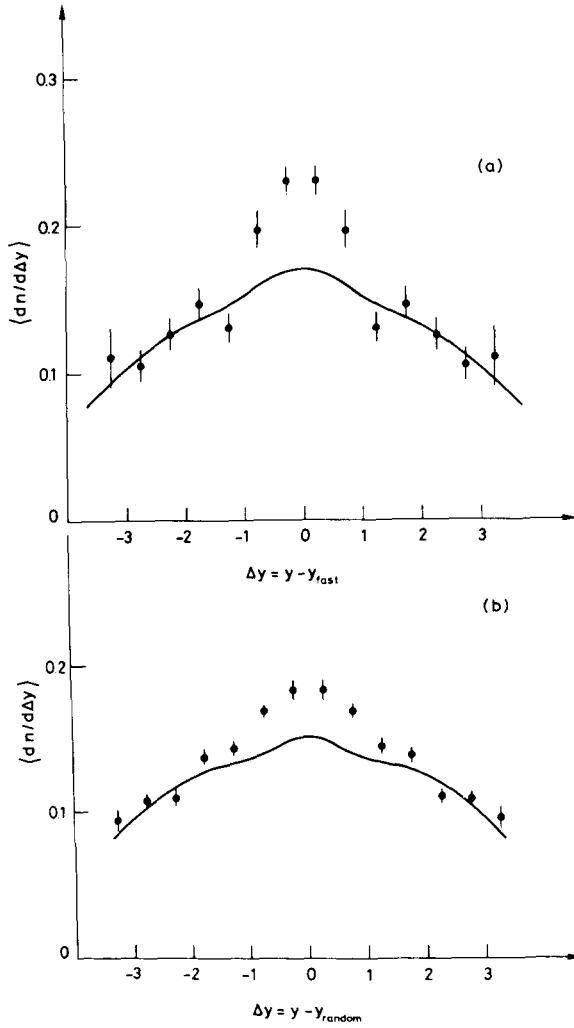


Fig. 16. (a) Average charged particle density in the interval $|y| < 1.5$ and $|\mathbf{180}^\circ - \phi| < 35^\circ$ for events with a large x_e particle having $p_x > 1.2$ GeV/c in the interval $|y_{fast}| < 1.5$ and $|\mathbf{180}^\circ - \phi_{fast}| < 35^\circ$. The fastest particle is not included in the plot. The particle density, which is a function of y and y_{fast} has been averaged over $y + y_{fast}$ and is displayed as a function of $y - y_{fast}$. Symmetric points around $y = y_{fast}$ have been combined to improve statistics. The line has the shape of the uncorrelated particle density and is normalized to the points at large values of $|y - y_{fast}|$. (b) Same distributions as in (a) when relaxing the requirement of having a large p_x particle. The reference particle is now chosen at random among secondaries with $p_x < 0.6$ GeV/c.

we repeat the same analysis, but relax the condition that a particle with a large p_x should be detected. We require instead that at least one particle with $p_x < 0.6 \text{ GeV}/c$ is observed and make it play the role of the large x_e particle. The excess extends now over $\pm(0.77 \pm 0.12)$ units of rapidity but contains only 0.18 ± 0.03 particles per event. The observation that similar rapidity correlations exist among the low p_x secondaries in a large p_t event as for minimum bias triggers had already been made previously [5]. The fact that larger correlations are found between the particle with the largest x_e (when this particle has in addition a large p_x) and the other secondaries is new. It may indicate an intrinsic symmetry between the side of the trigger and the opposite side.

Fig. 17 shows rapidity distributions of secondaries produced in an event where a large x_e particle is emitted with $0 < y < 1.5$ and $x_e > 0.4$. We have separated the cases where the secondary and the large x_e product have the same charge from those where they have opposite charges. After subtraction of a minimum bias back-

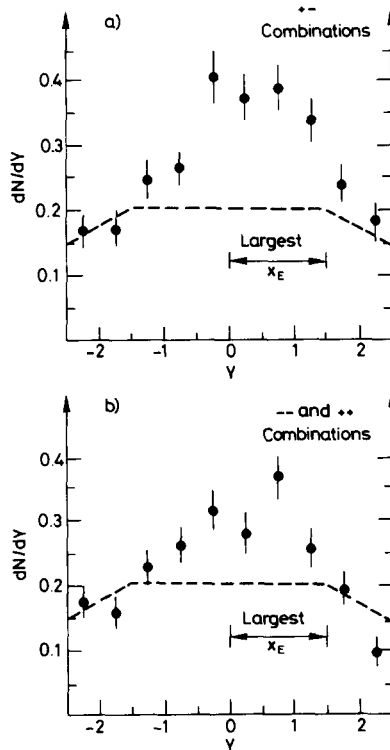


Fig. 17. Rapidity distributions of charged particles in the hemisphere opposite the π^0 from events in which a large x_e particle ($p_x > 1.2 \text{ GeV}/c$) is produced with $0 \leq y \leq 1.5$. The largest x_e particle is not included in the plots. (a) For secondaries having a charge opposite to that of the large x_e particle. (b) For secondaries having the same charge as the large x_e particle.

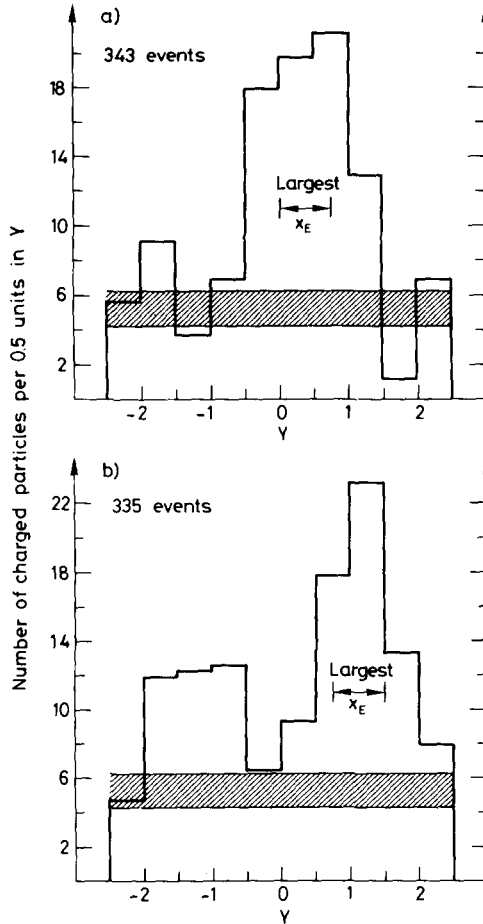


Fig. 18. Rapidity distributions of high p_x charged particles ($p_x > 0.8 \text{ GeV}/c$) from events in which the largest x_e particle ($p_x > 1.2 \text{ GeV}/c$) is within the rapidity intervals: (a) $0 \leq y \leq 0.75$, (b) $0.75 \leq y \leq 1.5$. The particle with the largest x_e is not included in the plots. The cross-hatched area is the distribution described in the text.

ground, as shown in the figure, we find, in addition to the large x_e particle, 0.64 ± 0.20 charged secondaries of which one third have the same charge as the large x_e particle and two thirds have the opposite charge.

Up to now we have considered all charged secondaries in the region opposite to the trigger π^0 without paying attention to the value of their transverse momentum. It would be instructive to repeat the above study for high p_t charged secondaries only, but the limited statistics and the relatively low value of $p_t^{\pi^0}$ render it difficult. As a step in this direction we have selected charged secondaries with $p_x > 0.8 \text{ GeV}/c$ and studied their rapidity distribution for two rapidity intervals

of the large x_e product. This is shown in fig. 18 where the cross-hatched distribution is calculated under the assumption that the large x_e product and the high p_x secondary are uncorrelated and distributed according to the $p_t^{\pi^0}$ spectrum and to the minimum bias distribution respectively. We observe a component strongly correlated with the large x_e product, which contains 0.15 ± 0.06 particles per event after subtraction of the above mentioned background. The rapidity range covered by the correlated particle is quite narrow. The minimum bias calculation gives an adequate description of the background outside the peak. However this comparison is not definitive because of poor statistics.

5. Conclusion

The combination, in the present experiment, of momentum analysis with large solid angle coverage has provided a deeper understanding of large p_t processes than had been previously possible. The results give further support to the picture, which had already emerged from previous data, according to which the event structure factorizes in three families of particles: an underlying “normal” event with low p_t products, and two sets of particles, emitted in regions of opposite azimuth, with properties directly related to the high p_t process.

The first of these two sets contains the large p_t trigger itself, in our case an identified π^0 , together with other particles produced at small angles to it. By observing the shrinkage of the rapidity distribution of these particles when their transverse momentum increases, we have shown that their invariant mass with the trigger π^0 , or equivalently their transverse momentum to the direction of the trigger π^0 , is limited. Such a behaviour would be expected if these particles, and the trigger π^0 itself, were decay products of a common parent. We indeed observed a strong ρ^\pm signal, corresponding to a production cross section similar to that of direct pions, but accounting for only a small part of the observed correlation. In addition we gave evidence for an important three particle rapidity correlation which excludes the possibility that the common parent, if it exists, always decays into only two particles.

The second set is confined to an azimuthal region opposite to that of the trigger π^0 , and is at first sight of a different nature in that it inclusively covers a much wider rapidity range. This is however no longer true when investigated on an event to event basis: we have shown evidence for a narrow rapidity clustering of large p_t products in this azimuthal region. In addition, we have observed that the momentum out of the scatter plane was limited to a value of half a GeV/c generating a shrinkage of the azimuthal distribution when the trigger momentum increases. These new and important properties point to similarities between the two sets which were not previously apparent. Another salient feature of the data in this azimuthal region is exhibited by the transverse momentum sharing among the collision products which we find strikingly similar to analogous hadronic distributions

measured in electro production and in e^+e^- collisions.

When considered together, these properties are surprisingly reminiscent of the coplanar two-jet picture first given by Berman, Bjorken and Kogut [1] in the frame of quark parton models. Further evidence for or against this interpretation would require a trigger with a larger transverse momentum than available in the present experiment in order to better isolate in phase space the collision products directly involved in the high p_t process. In addition triggering on total transverse momentum over a wide angular region would avoid possible biases in the decay configuration of the jet on the trigger side.

We are very much indebted to Professor J. Steinberger for his constant interest and encouragement.

Our group has been fortunate enough to have benefitted from the efforts of the very many people who have worked on making the SFM Detector and its associated software programs a working system. The number of people to whom we owe a debt of gratitude is therefore much too large to name. We wish however to single out for thanks the SFMD Group and the CHOV Collaboration for their help during the installation of our equipment and data taking, and the CERN Data Division's SFM Programming Group for its constant help with software programs used in processing our data.

We thank Professors G.R. Farrar, M. Jacob and P.V. Landshoff for several stimulating discussions.

References

- [1] S.M. Berman, J.D. Bjorken and J.B. Kogut, *Phys. Rev.* 4D (1971) 3388;
P.V. Landshoff, Plenary report on large transverse momentum reactions, Proc. 17th Int. Conf. on high-energy physics, London 1974, p.v. 57;
S.D. Ellis, Theoretical models for large transverse momentum phenomena, Proc. 17th Int. Conf. on high-energy physics, London, 1974, p.V. 23;
D. Sivers, S.J. Brodsky and R. Blankenbecler, *Phys. Reports* 23 (1976) 1.
- [2] A. Jabs, *Nuovo Cimento Letters* 9 (1974) 570;
S. Pokorski and L. Van Hove, CERN preprints TH-1565, 1930 (1974);
E.L. Berger and D. Bronson, *Phys. Letters* 45B (1973) 57;
P. Carruthers and M. Duong-Van, *Phys. Rev. Letters* 21 (1973) 133;
Meng Ta Chung, *Phys. Rev.* D9 (1974) 3062;
A. Bouquet, J. Letessier and A. Tonusi, *Physics Letters* 51B (1974) 235.
- [3] A.P. Contogouris and D. Schiff, Correlations at large transverse momenta, CERN preprint TH-2029, 1975.
- [4] P. Darriulat, Hadronic collisions with a large transverse momentum product, rapporteur talk at the Int. Conf. on high-energy physics, Palermo, Italy, June 1975.
- [5] K. Eggert et al., *Nucl. Phys.* B98 (1975) 73.
- [6] G. Finocchiaro et al., *Phys. Letters* B50 (1974) 396.
- [7] F.W. Büsser et al., High transverse momentum phenomena involving π and η mesons at the CERN ISR, paper presented at the Int. Symp. on leptons and photons, Stanford University, 21–27 August 1975;
F.W. Büsser et al., *Phys. Letters* 51B (1974) 306, 311.

- [8] K. Eggert et al., Nucl. Phys. B98 (1975) 49.
- [9] R. Bouclier et al., Nucl. Instr. 115 (1974) 235.
- [10] M. Holder et al., Nucl. Instr. 108 (1973) 541.
- [11] P. Darriulat et al., to be published.
- [12] R. Bouclier et al., Nucl. Instr. 125 (1975) 19.
- [13] H. Grote, A. Hivernat, M. Metcalf, C. Onions and F. Ranjard, A user's guide to the SFM off-line program chain, OM development AP-18, November 1975, unpublished, and references therein.
- [14] B. Alper et al., Nucl. Phys. B87 (1975) 19.
- [15] Particle data group, Phys. Letters 50B (1974) 78.
- [16] P. Capiluppi et al., Nucl. Phys. B79 (1974) 189.
- [17] J.T. Dakin et al., Phys. Rev. D10 (1974) 1401.
- [18] G.J. Feldman and M.L. Perl, Phys. Reports 19 (1975) 233;
B. Richter, Plenary report on $e^+e^- \rightarrow$ hadrons, Proc. 17th Int. Conf. on high-energy physics, London 1974, p. IV-37;
R. Hollebeek, LBL 3874 (May 1975) unpublished.